Biomedical Optics EXPRESS

Three-dimensional printed optical phantoms with customized absorption and scattering properties

Phuong Diep,[1,5] Sanjana Pannem,[1,5] Jordan Sweer,[1,5] Justine Lo,[1] Michael Snyder,[1] Gabriella Stueber,[1] Yanyu Zhao,[1] Syeda Tabassum,[2] Raeef Istfan,[1] Junjie Wu,[3] Shyamsunder Erramilli,[1,4] and Darren Roblyer[1,*]

[1]*Department of Biomedical Engineering, Boston University, Boston, MA 02115, USA*
[2]*Department of Electrical Engineering, Boston University, Boston, MA 02115, USA*
[3]*Department of Biology, Boston University, Boston, MA 02115, USA*
[4]*Department of Physics, Boston University, Boston, MA 02115, USA*
[5]*These authors contributed equally to this work*
[*]*roblyer@bu.edu*

Abstract: Three-dimensional (3D) printing offers the promise of fabricating optical phantoms with arbitrary geometry, but commercially available thermoplastics provide only a small range of physiologically relevant absorption (μ_a) and reduced scattering (μ_s`) values. Here we demonstrate customizable acrylonitrile butadiene styrene (ABS) filaments for dual extrusion 3D printing of tissue mimicking optical phantoms. $\mu_a$ and $\mu_s$` values were adjusted by incorporating nigrosin and titanium dioxide (TiO_2) in the filament extrusion process. A wide range of physiologically relevant optical properties was demonstrated with an average repeatability within 11.5% for μ_a and 7.71% for μ_s`. Additionally, a mouse-simulating phantom, which mimicked both the geometry and optical properties of a hairless mouse with an implanted xenograft tumor, was printed using dual extrusion methods. 3D printed tumor optical properties matched the live tumor with less than 3% error at a wavelength of 659 nm. 3D printing with user defined optical properties may provide a viable method for durable optically diffusive phantoms for instrument characterization and calibration.

OCIS codes: (170.5280) Photon migration; (110.0113) Imaging through turbid media; (110.7050) Turbid media; (160.4670) Optical materials.

References and links

1. B. W. Pogue and M. S. Patterson, "Review of tissue simulating phantoms for optical spectroscopy, imaging and dosimetry," J. Biomed. Opt. **11**(4), 041102 (2006).
2. A. E. Cerussi, R. Warren, B. Hill, D. Roblyer, A. Leproux, A. F. Durkin, T. D. O'Sullivan, S. Keene, H. Haghany, T. Quang, W. M. Mantulin, and B. J. Tromberg, "Tissue phantoms in multicenter clinical trials for diffuse optical technologies," Biomed. Opt. Express **3**(5), 966–971 (2012).
3. G. Quarto, A. Pifferi, I. Bargigia, A. Farina, R. Cubeddu, and P. Taroni, "Recipes to make organic phantoms for diffusive optical spectroscopy," Appl. Opt. **52**(11), 2494–2502 (2013).
4. R. Cubeddu, A. Pifferi, P. Taroni, A. Torricelli, and G. Valentini, "A solid tissue phantom for photon migration studies," Phys. Med. Biol. **42**(10), 1971–1979 (1997).
5. S. Merritt, G. Gulsen, G. Chiou, Y. Chu, C. Deng, A. E. Cerussi, A. J. Durkin, B. J. Tromberg, and O. Nalcioglu, "Comparison of water and lipid content measurements using diffuse optical spectroscopy and MRI in emulsion phantoms," Technol. Cancer Res. Treat. **2**(6), 563–569 (2003).
6. G. J. Greening, R. Istfan, L. M. Higgins, K. Balachandran, D. Roblyer, M. C. Pierce, and T. J. Muldoon, "Characterization of thin poly(dimethylsiloxane)-based tissue-simulating phantoms with tunable reduced scattering and absorption coefficients at visible and near-infrared wavelengths," J. Biomed. Opt. **19**(11), 115002 (2014).
7. T. T. Nguyen, H. N. Le, M. Vo, Z. Wang, L. Luu, and J. C. Ramella-Roman, "Three-dimensional phantoms for curvature correction in spatial frequency domain imaging," Biomed. Opt. Express **3**(6), 1200–1214 (2012).
8. J. Wang, J. Coburn, C. P. Liang, N. Woolsey, J. C. Ramella-Roman, Y. Chen, and T. J. Pfefer, "Three-dimensional printing of tissue phantoms for biophotonic imaging," Opt. Lett. **39**(10), 3010–3013 (2014).

#246142 Received 28 Jul 2015; revised 24 Sep 2015; accepted 29 Sep 2015; published 2 Oct 2015

9. D. J. Cuccia, F. Bevilacqua, A. J. Durkin, F. R. Ayers, and B. J. Tromberg, "Quantitation and mapping of tissue optical properties using modulated imaging," J. Biomed. Opt. **14**(2), 024012 (2009).
10. M. Martinelli, A. Gardner, D. Cuccia, C. Hayakawa, J. Spanier, and V. Venugopalan, "Analysis of single Monte Carlo methods for prediction of reflectance from turbid media," Opt. Express **19**(20), 19627–19642 (2011).
11. R. P. Singh-Moon, D. M. Roblyer, I. J. Bigio, and S. Joshi, "Spatial mapping of drug delivery to brain tissue using hyperspectral spatial frequency-domain imaging," J. Biomed. Opt. **19**(9), 096003 (2014).
12. S. Gioux, A. Mazhar, D. J. Cuccia, A. J. Durkin, B. J. Tromberg, and J. V. Frangioni, "Three-dimensional surface profile intensity correction for spatially modulated imaging," J. Biomed. Opt. **14**(3), 034045 (2009).
13. R. B. Saager, A. Truong, D. J. Cuccia, and A. J. Durkin, "Method for depth-resolved quantitation of optical properties in layered media using spatially modulated quantitative spectroscopy," J. Biomed. Opt. **16**(7), 077002 (2011).
14. T. Durduran, R. Choe, J. P. Culver, L. Zubkov, M. J. Holboke, J. Giammarco, B. Chance, and A. G. Yodh, "Bulk optical properties of healthy female breast tissue," Phys. Med. Biol. **47**(16), 2847–2861 (2002).
15. A. Cerussi, N. Shah, D. Hsiang, A. Durkin, J. Butler, and B. J. Tromberg, "In vivo absorption, scattering, and physiologic properties of 58 malignant breast tumors determined by broadband diffuse optical spectroscopy," J. Biomed. Opt. **11**(4), 044005 (2006).
16. S. C. Gebhart, W. C. Lin, and A. Mahadevan-Jansen, "In vitro determination of normal and neoplastic human brain tissue optical properties using inverse adding-doubling," Phys. Med. Biol. **51**(8), 2011–2027 (2006).
17. S. L. Jacques, "Optical properties of biological tissues: a review," Phys. Med. Biol. **58**(11), R37–R61 (2013).
18. K. E. Michaelsen, V. Krishnaswamy, A. Shenoy, E. Jordan, B. W. Pogue, and K. D. Paulsen, "Anthropomorphic breast phantoms with physiological water, lipid, and hemoglobin content for near-infrared spectral tomography," J. Biomed. Opt. **19**(2), 026012 (2014).
19. J. S. Miller, K. R. Stevens, M. T. Yang, B. M. Baker, D. H. Nguyen, D. M. Cohen, E. Toro, A. A. Chen, P. A. Galie, X. Yu, R. Chaturvedi, S. N. Bhatia, and C. S. Chen, "Rapid casting of patterned vascular networks for perfusable engineered three-dimensional tissues," Nat. Mater. **11**(9), 768–774 (2012).

1. Introduction

Dependable tissue-simulating phantoms are necessary for many optical imaging and spectroscopy applications, and often occupy a key role in system development, calibration, multi-center trials, and the testing of new imaging protocols [1,2]. The complexity and variability of applications require a wide range of phantom materials and material optical properties. To date, most published phantom fabrication methods utilize either liquids or solidified materials, often limiting the ability to control the geometry of the final product. As an example, agar, silicone, and resins are commonly used as a matrix substrate for solid phantoms with absorbing dyes and scattering agents added prior to curing [3–6]. 3D printing has emerged as a novel method for fabricating objects of arbitrary geometry, and thereby allows for the creation of a wide-range of optical phantoms for imaging and spectroscopy applications at many spatial scales.

There is limited prior work applying 3D printing and rapid prototyping technologies to optical phantom fabrication. Nguyen *et. al.* used 3D printed thermoplastic phantoms for curvature correction during Spatial Frequency Domain Imaging (SFDI) [7]. More recently, Wang *et. al.* demonstrated both thermosoftening- and photopolymerization-based rapid prototyping techniques for creating tissue-like optical phantoms for hyperspectral imaging applications with a focus on the microstructure of the resulting phantoms and the development of water-tight embedded channels with diameters ranging from 100 μM to 2 mm [8]. A key step in improving the versatility of 3D printed optical phantoms is the ability to alter the raw materials' optical absorption coefficient, μ_a, and reduced scattering coefficient, $\mu_s`$, to match that of a known target tissue. A rapid and consistent methodology to generate this raw material would allow the fabrication of phantoms for specific applications. The importance of this development would be compounded by the ability to spatially vary the optical properties throughout a 3D printed phantom.

The purpose of this study was to move towards fully engineered optical phantoms in regards to the following three criteria: 1) designed phantom geometry in three dimensions, 2) customizable μ_a and $\mu_s`$ of raw printing materials and 3) spatially varying optical properties within a 3D printed phantom. While 1) is an intrinsic characteristic of 3D printing, both 2) and 3) are novel in the realm of rapid prototyping of tissue-simulating optical phantoms. In order to move towards the goals of fully customized optical phantoms, we present here a methodology for varying the optical properties of the most commonly used 3D printing thermoplastic, acrylonitrile butadiene styrene (ABS), by utilizing the addition of an absorbing

#246142 Received 28 Jul 2015; revised 24 Sep 2015; accepted 29 Sep 2015; published 2 Oct 2015

dye, nigrosin, and a scattering agent, titanium dioxide, to the raw ABS material prior to extrusion. The ability of this customized filament to produce optical phantoms with high repeatability and with physiologically relevant optical properties was demonstrated through the fabrication of a matrix of printed phantoms with different mass fractions of absorbing and scattering agents. Additionally, to demonstrate the ability to spatially vary the optical properties of a 3D printed phantom, a live mouse with an implanted xenograft tumor was scanned using optical profilometry and optically measured using Spatial Frequency Domain Imaging (SFDI) in the visible and near infrared wavelength regimes (470 nm – 851 nm). Then, both the 3-dimensional geometry of the mouse as well as the tumor optical properties of the mouse were recreated using dual extrusion 3D printing with custom filament, which uses two extruders, each extruding a filament with a single set of optical properties. Relatively inexpensive materials and hobby-level 3D printers were used for all procedures.

2. Materials and methods

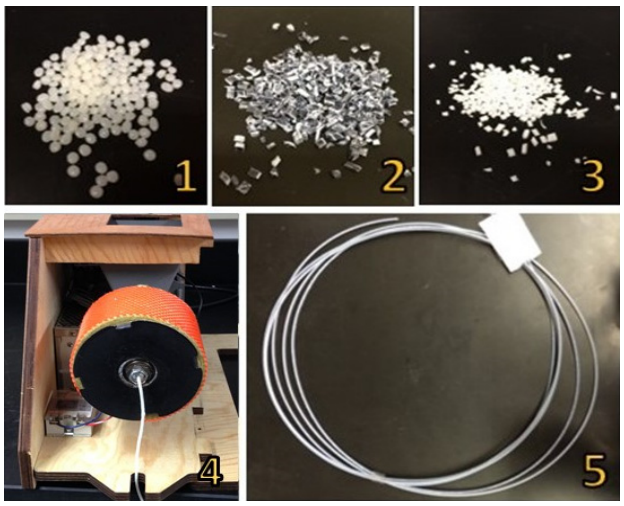

Fig. 1. Raw materials for custom 3D printing filament. (1) ABS pellets, (2) nigrosin chips of 2 x 2 mm, (3) TiO_2 chips of 2 x 2 mm, and (4) Filabot Wee extruder. The resulting filament of 1.75 mm in diameter is illustrated in (5).

2.1 Filament fabrication

Custom filament suitable for 3D printing was fabricated by co-extruding a mixture of commercially available natural color ABS pellets (Filabot, Montpelier, VT) with custom absorption and scattering ABS "chips" (Fig. 1.1-1.3). These chips were made by combining ABS with either the absorbing dye nigrosin or the scattering agent titanium dioxide (TiO_2), both of which have been used in other optical phantom recipes [1]. Fabrication of TiO_2 chips consisted of the following steps: 20 g of ABS pellets were dissolved in 50 ml of acetone for at least 12 hours. In a separate container, 0.2 g of TiO_2 was mixed with 1000 µl of tap water and sonicated for 10 minutes, with up to 5 additional minutes if heterogeneities were persistent. 1000 µl of acetone was then added in 200 µl increments to prevent precipitation of TiO_2. The TiO_2 solution was gradually added to the ABS mixture and was stirred vigorously to create a homogeneous solution. The mixture was then poured into a 21 × 21 cm pan to a layer thickness of 1.5 mm and vacuumed to remove air bubbles. Vacuuming consisted of an 80 kPa vacuum for 1 min followed by a reduced 40 kPa vacuum for 1-2 seconds. This was repeated until all visible bubbles were eliminated. The pan and ABS/TiO_2 solution were left in the 40 kPa vacuum overnight to dry and solidify. Once completely solidified, the thin sheet was cut with scissors into small chips approximately 2 × 2 mm in dimension (Fig. 1.3). Nigrosin chips were created using the same protocol described above but replacing the TiO_2 solution with a solution of 0.02 g of nigrosin and 800 µl tap water. The ratio of nigrosin/TiO_2 chips to ABS

#246142 Received 28 Jul 2015; revised 24 Sep 2015; accepted 29 Sep 2015; published 2 Oct 2015

pellets in a specific filament was specified by mass ratio. A commercially available plastic extruder (Wee Extruder, Filabot, Montpelier, VT) was used to extrude custom filaments (Fig. 1.4). Each extrusion required a total material mass of 30 g and the die temperature was set to 181.5 C. Nigrosin and TiO_2 chips were mixed together prior to extrusion in the desired mass ratio. Each was apportioned into smaller samples and then added to the hopper regularly throughout the extrusion process to provide a more homogenous filament product. One extruding session took approximately 15 minutes and was terminated when the filament reduced in diameter as the raw material in the hopper diminished. Two different filament diameters were extruded (1.75 mm and 2.3 mm) to accommodate 3D printing on two separate printers, each used for different experiments. A 30 g batch of raw ABS pellets and chips yielded approximately two 2 × 2 × 2 cm 3D printed cubes.

2.2 3D printing of custom filament

Twelve 2 × 2 × 2 cm cubes, each with a different combination of μ_a and $\mu_s`$, were 3D printed using custom filament to demonstrate a range of physiological relevant optical properties. The dimensions of the cubes were chosen to be sufficiently large (cm scale) so as to allow optical property determination using diffuse optical imaging techniques with minimal edge effects. A STereoLithography (STL) file of the cube was created in SolidWorks (Dassault Systèmes, Vélizy, France) and Makerware (MakerBot Industries, Brooklyn, NY) was used to generate the G-code for printing. Repeatability was demonstrated by making several cubes with the same recipe. For two different nigrosin and TiO_2 concentrations (0.0025% nigrosin/0.20% TiO_2 and 0.0075% nigrosin/0.10% TiO_2), three separate filaments were extruded in three extrusion sessions to produce three different cubes with the same target optical properties. These matched cubes were analyzed to determine the variation of optical properties between different extrusions.

A mouse phantom was created to demonstrate a relevant small animal mimic suitable for wide-field imaging. The phantom replicated the physical geometry of a SCID Hairless mouse with a subcutaneously implanted prostate xenograft tumor on the flank. Two custom filaments were used to print the mouse, one matching the average optical properties of the tumor and the other made of pure natural ABS plastic. A 3D model of the live anesthetized mouse was generated using a commercial optical 3D scanning system and an automated rotation stage (David 3D, Koblenz, Germany). The resulting STL file was imported into the Blender software package (Blender Foundation, Amsterdam, Netherlands) and the tumor was digitally separated from the mouse body and both were exported as separate STL files. Matter Control (MatterHackers Inc., Lake Forest CA) was then used to combine and slice the STL files (tumor and mouse body), a step necessary for dual extrusion 3D printing. All animal experimental procedures were approved by the Boston University IACUC.

All 3D prints were done with either a MakerBot Replicator 2X or Airwolf3D AW3D HDR. The MakerBot printer had the following settings: 230 C extruder temperature, 115 C bed temperature, 0.2 mm layer thickness, 1.75 mm filament diameter, and 85% infill density. Typically, a raft was built to ensure the printed object was firmly affixed to the platform. For the Airwolf Printer, the layer thickness and infill density were equivalent to those specified above while the extruder temperature and the bed temperature were set to 220 C and 110 C with a 2.3 mm filament diameter. The mouse phantom print required extruder and bed temperatures of 215 C and 120 C.

2.3 Determination of optical properties

Optical properties of the cubes, the live mouse, and the mouse phantom were measured using Spatial Frequency Domain Imaging (SFDI). SFDI is capable of spatially mapping optical properties over a wide-field. Briefly, the optical modulation transfer function of a diffusive media is measured in the spatial frequency domain. Calibrated diffuse reflectance maps at each illumination spatial frequency and wavelength are then fed to an inverse model to extract optical properties [9–11]. A commercially available SFDI system (OxImager RS, Modulated Imaging Inc., Irvine, CA) was used for this study and the acquisition parameters provided μ_a

#246142 Received 28 Jul 2015; revised 24 Sep 2015; accepted 29 Sep 2015; published 2 Oct 2015

and μ_s` maps at 8 different wavelengths: 471, 526, 591, 621, 659, 691, 731 and 851 nm over a 15cm × 15cm field-of-view. The spatial frequencies utilized for model fitting were 0, 0.05, 0.1, 0.15, and 0.2 $mm^{-1}$. A refractive index of 1.4 was assumed for all measurements. Average $\mu_a$ and $\mu_s$` values for each cube as well as the tumor and normal region of the live mouse and mouse phantom were extracted from 2D absorption and scattering maps using ImageJ (NIH). A square region-of-interest (ROI) of 1000-1500 pixels (0.82 cm^2-1.22 cm^2) was selected from each cube to determine the average and standard deviation of both μ_a and μ_s`. Each ROI was chosen to avoid edge artifacts. For both the live mouse and the mouse phantom, ROI's were selected over the tumor to extract average $\mu_a$ and $\mu_s$` values. To correct for the complicated mouse geometry, the SFDI implemented a height correction algorithm during data acquisition [12]. The custom filaments used to fabricate the mouse phantom were chosen to match the live mouse tumor optical properties as closely as possible.

3. Results

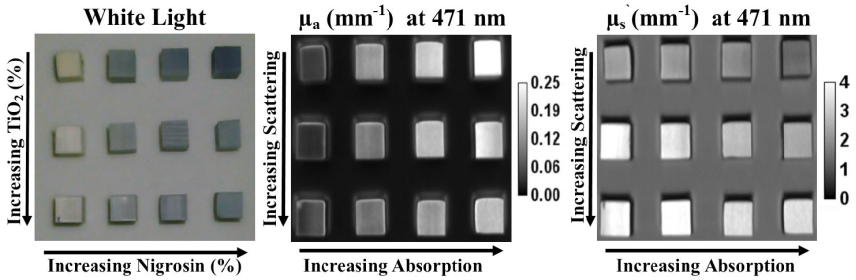

Fig. 2. White light image (left), and SFDI maps of absorption (middle) and reduced scattering (right) at 471 nm.

Table 1: Mean ± standard deviation μ_a and μ_s` values for all cubes at 471nm.

		Nigrosin (%)							
		0%		0.0025%		0.0050%		0.0075%	
		μ_a (mm^{-1})	μ_s` (mm^{-1})	μ_a (mm^{-1})	μ_s` (mm^{-1})	μ_a (mm^{-1})	μ_s` (mm^{-1})	μ_a (mm^{-1})	μ_s` (mm^{-1})
TiO_2 (%)	0%	0.043 ± 0.002	2.23 ± 0.05	0.135 ± 0.006	2.13 ± 0.09	0.192 ± 0.008	1.87 ± 0.09	0.304 ± 0.015	1.34 ± 0.06
	0.10%	0.030 ± 0.002	3.82 ± 0.40	0.101 ± 0.006	3.42 ± 0.23	0.172 ± 0.003	2.78 ± 0.06	0.205 ± 0.023	2.43 ± 0.05
	0.20%	0.054 ± 0.010	3.98 ± 0.10	0.093 ± 0.005	4.16 ± 0.17	0.135 ± 0.006	3.43 ± 0.07	0.172 ± 0.004	3.39 ± 0.06

Figure 2 shows the matrix of cubes in white light as well as μ_a and μ_s` maps at 471 nm. Table 1 shows the corresponding $\mu_a$ and $\mu_s$` values of the cubes at 471nm. The color balance was adjusted to improved visualization of the white light image. The white light image shows how cubes were aligned in the matrix, with nigrosin concentration increasing from left to right (0%, 0.0025%, 0.0050% and 0.0075% by mass with precision of ± 0.0005%) and TiO_2 increasing from top to bottom (0%, 0.10% and 0.20% by mass with precision of ± 0.01%). The optical property maps show the range of μ_a (0.030 ± 0.002 to 0.304 ± 0.015 mm^{-1}) and μ_s` (1.34 ± 0.06 to 4.16 ± 0.17 $mm^{-1}$) for the customized filaments at 471 nm. The relative consistency in values in each column of the $\mu_a$ map and each row of the $\mu_s$` map validates the independent relationship between absorption and nigrosin concentrations and scattering and TiO_2 concentrations. Figure 3 shows the mean and standard deviation of both μ_a and μ_s` for each cube at all 8 wavelengths and Fig. 4 shows the average $\mu_a$ and $\mu_s$` versus mass fraction of nigrosin and TiO_2 at three representative wavelengths. The general spectral shape of

#246142 Received 28 Jul 2015; revised 24 Sep 2015; accepted 29 Sep 2015; published 2 Oct 2015

absorption in all cubes containing nigrosin in Fig. 3 generally matches the spectral shape of nigrosin in water, which has a peak in μ_a near 600 nm [13]. Both subplots in Fig. 4 demonstrate a strong correlation between nigrosin, TiO_2, and μ_a and $\mu_s`$ respectively. Absorption and scattering demonstrate a strong linear correlation with nigrosin and TiO_2 at 851 nm with an R^2 value of 0.9994 and 0.9755. The weakest correlation was at 659 nm for absorption with an R^2 value of 0.9724 and at 471 nm for scattering with a R^2 value of 0.9664.

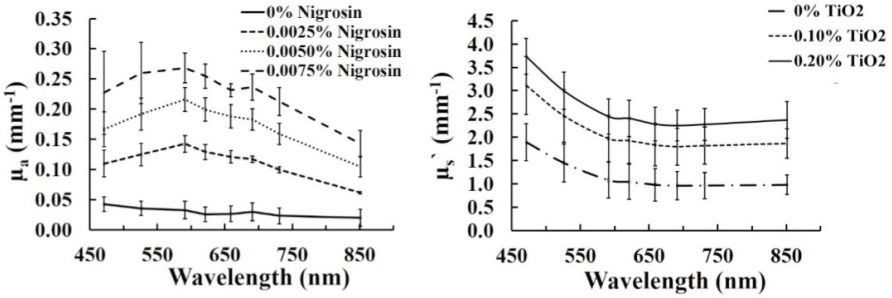

Fig. 3. Absorption, averaged over all TiO_2 concentrations, and reduced scattering, averaged over all nigrosin concentrations, of all 3D printed cubes for 471, 526, 591, 621, 659, 691, 731 and 851 nm.

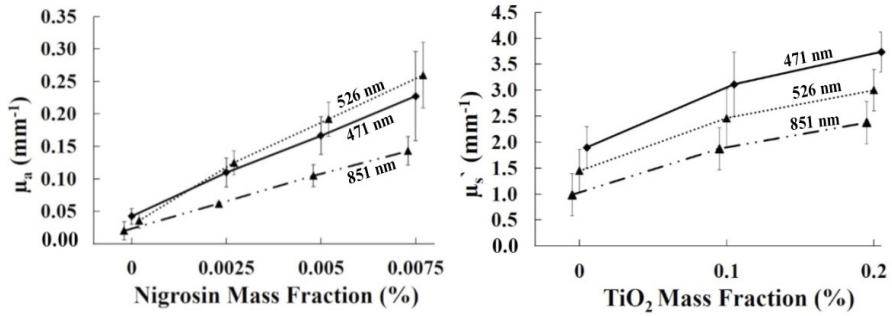

Fig. 4. Absorption and reduced scattering for different nigrosin and titanium dioxide (TiO_2) mass fractions at three representative wavelengths. Data points are slightly offset of the x-axis values for clarity in error bars.

Repeatability was tested at two concentrations: (1) 0.0025% ± 0.0005% nigrosin with 0.20% ± 0.01% TiO_2 and (2) 0.0075% ± 0.0005% nigrosin with 0.10% ± 0.01% TiO_2. Three cubes were made for each concentration, each from a separate printing and extruding session, but with identical fabrication parameters (die temperature, infill density, etc.). Repeatability was determined for μ_a and $\mu_s`$ per wavelength. Defining repeatability as the percent standard deviation in optical properties over the three cubes, for the first concentration, the highest and lowest repeatability for μ_a occurred at 621 and 851 nm, with values of 3.07% and 15.9% respectively. The highest and lowest repeatability for $\mu_s`$ occurred at 471 and 851 nm, with values of 1.80% and 15.9% respectively. The $\mu_a$ and $\mu_s`$ repeatability values, calculated at each wavelength, were then averaged to yield a mean repeatability of 6.23% and 7.71% respectively. For the second concentration, the highest and lowest repeatability for μ_a occurred at 471nm and 851nm, with values of 7.16% and 15.4% respectively. The highest and lowest repeatability for $\mu_s`$ was at wavelengths 471 and 851 nm, with values of 1.13% and 2.13% respectively. The $\mu_a$ and $\mu_s`$ repeatability values, calculated at each wavelength, were then averaged to yield a mean repeatability of 11.5% and 1.63% respectively. No trends in repeatability error were observed over wavelength.

#246142 Received 28 Jul 2015; revised 24 Sep 2015; accepted 29 Sep 2015; published 2 Oct 2015

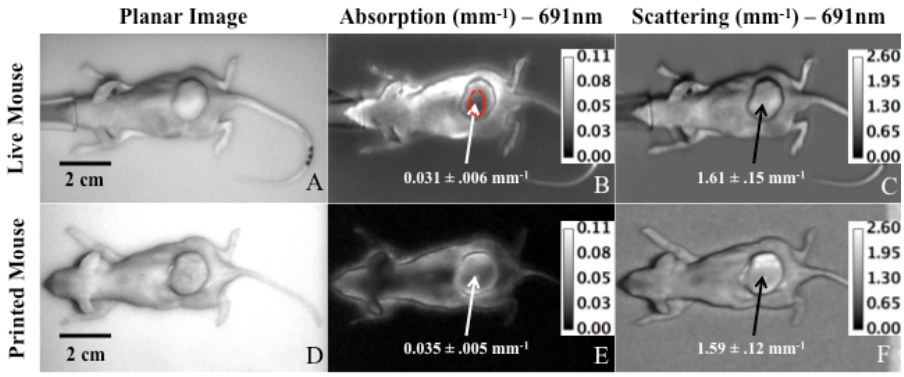

Fig. 5. Planar images, μ_a maps, and $\mu_s`$ maps of the live and printed mouse at 691 nm. The red circle in (B.) shows the user defined ROI of 380 pixels (0.31cm^2) used to calculate average optical properties of the tumors. An identical ROI was used for 5B-C and 5E-F. The live and custom mice were imaged on different background phantoms.

Figures 5(A)-5(C) displays a planar image, a μ_a map, and a $\mu_s`$ map for the live mouse at 691 nm while Figs. 5(D)-5(F) show the same data for the printed mouse. An elliptical ROI of 380 pixels (0.31 cm$^2$) was selected over the flat area of the tumor for optical measurements of $\mu_a$ and $\mu_s`$, as shown in Fig. 5(B). Filament consisting of 0.00125% nigrosin and 0.0500% TiO_2 was used to simulate tumor optical properties and natural ABS was extruded to represent the normal tissue. Spatially varied optical properties within a single phantom (tumor versus normal tissue) were accomplished using dual extrusion printing. Table 2 shows the height corrected optical properties of both the live and custom mouse tumors at 659, 691, 731, and 851 nm. The printed tumor μ_a values matched the xenograft tumor within 2.6% at 659 nm, 12.9% at 691 nm, 3.6% at 731 nm, and 37.5% at 851 nm. $\mu_s`$ values matched within 2.0% for all four wavelengths. A 2-sample equivalence test was conducted to confirm the agreement in optical properties between the live and printed mouse tumor using Minitab 17 (Minitab, State College, PA). Unlike a student's t-test, which tests whether the means of two data sets are different, the equivalence test assess whether the means are equivalent within a user-defined threshold. A p-value less than alpha (0.05 for this study) rejects the null hypothesis that the two means are not equivalent within the user-defined equivalence interval. For absorption at both 659 nm and 731 nm, the equivalence test yielded a p-value <0.001 when tested with a threshold value of 5% of the mean live mouse value, indicating equivalent means. For 691 nm and 851 nm, p-values were >0.999, indicating different absorption means. All four wavelengths showed p-values of <0.001 for scattering. The normal (non-tumor) tissue, printed with natural ABS (0% nigrosin, 0% TiO_2), yielded μ_a and $\mu_s`$ consistent with the natural ABS cube measurement from Fig. 3, producing, for example, $\mu_a$ and $\mu_s`$ values of 0.017 ± 0.003 mm^{-1} and 1.32 ± 0.11 mm^{-1} at 659 nm.

Table 2. Mean ± standard deviations of μ_a and $\mu_s`$ for the live and custom printed mouse.

Wavelength	Live Mouse Tumor		Printed Mouse Tumor: 0.00125% Nigrosin 0.0500% TiO_2	
	μ_a (mm^{-1})	$\mu_s`$ (mm^{-1})	μ_a (mm^{-1})	$\mu_s`$ (mm^{-1})
659 nm	0.039 ± 0.007	1.61 ± 0.14	0.038 ± 0.005	1.64 ± 0.12
691 nm	0.031 ± 0.006	1.61 ± 0.15	0.035 ± 0.005	1.59 ± 0.12
731 nm	0.028 ± 0.005	1.58 ± 0.15	0.027 ± 0.004	1.58 ± 0.12
851 nm	0.024 ± 0.004	1.60 ± 0.17	0.015 ± 0.002	1.61 ± 0.14

#246142 Received 28 Jul 2015; revised 24 Sep 2015; accepted 29 Sep 2015; published 2 Oct 2015

4. Conclusion

Prior investigations exploring fabrication methods for 3D printed optical phantoms have demonstrated the ability to fabricate μm to cm scale phantom geometries, including micro flow channels and mouse phantoms [7,8]. A major limitation in these studies was that the phantoms produced were homogenous, with optical properties determined by the native filament or photopolymer. Our work provides, to the best of our knowledge, the first successful demonstration of customized optical properties with dual extrusion 3D printing for optical phantom fabrication. The study identified a repeatable methodology for producing extrudable ABS filament by adding the absorbing dye nigrosin and the scattering agent TiO_2. Bulk optical properties were successfully controlled by adjusting the mass percentage of these two additives during extrusion and repeat prints produced matching optical properties within 11.5% on average. Diffuse optical imaging of simple homogenous cubic structures and more complex heterogeneous organism-mimicking prints demonstrated the potential of this technique to reproduce a range of biological scenarios. As a demonstration, a mouse phantom mimicking the physical geometry and optical properties of a live mouse with a prostate xenograft tumor was fabricated with optical properties of the printed and live tumor matching within 3% at 659 nm.

Several key areas are open to improvement in this area. First, the native absorption and scattering of "natural" color ABS are relatively high compared to some biological tissues in the visible and near-infrared wavelength regimens. For example, the μ_a at 659 nm of the natural ABS was approximately 0.016 mm^{-1} and increased to 0.133 mm^{-1} with the addition of even small amounts of nigrosin. In comparison, breast tissue has been reported to be approximately 0.005 mm^{-1} (normal tissue at 750 nm) and 0.010 mm^{-1} (tumor tissue at 650 nm) [14,15]. The range of absorption overlaps well with reported absorption for white and grey brain matter, which has been reported as approximately 0.07 – 0.08 mm^{-1} at 670 nm [16]. The lowest $\mu_s`$ value measured for the natural ABS was 1.34 $mm^{-1}$ at 659 nm, which approximates values for breast tissue (1.27 $mm^{-1}$ at 650 nm) and brain tissue (1.59 $mm^{-1}$ at 650 nm) reported by a meta-analysis by Jacques [17]. Higher $TiO_2$ mass percentages provided $\mu_s`$ values that approached some reported white brain matter scattering values (5 mm^{-1} at 670 nm) [16]. Exploration of other raw materials with lower intrinsic μ_a and $\mu_s`$ values may provide the ability to mimic more tissue types, and other authors have shown that polypropylene-like low turbidity photopolymers (LTPP) have somewhat lower native $\mu_a$ and $\mu_s`$ [8]. Other areas open to improvement include an increased ability to spatially vary optical properties, which was limited by the dual extrusion process in this study, as it allowed only two sets of optical properties per print. Additionally, the effects of layer thickness, infill pattern, and infill density on bulk optical properties are likely to be nontrivial and, while deserving of further exploration and characterization, extend beyond the scope of this work.

Several potential applications for customized 3D printed phantoms include optical system characterization, which often utilize embedded inclusions of various dimension and depths to quantify the depth penetration of an optical system. Phantoms of graded or discretely varying optical properties would be useful for evaluating the ability of time and frequency domain diffuse optical systems to separate absorption and scattering of diffusive media. Hollow and water-tight inclusions that can also mimic vasculature would allow for liquid fluorophores or hemoglobin containing liquids to be combined with complex geometric solid phantoms.

In the future, the use of more biologically compatible materials may allow for more complex and biologically relevant 3D printed structures. For example, lipid, water, and hemoglobin were recently used to fabricate anthropomorphic phantoms mimicking the complex tissue geometry of human breast tissue [18]. Additionally, 3D printing of biocompatible carbohydrate glass was recently used to create vascular-like networks, which sustained the metabolic function of hepatocytes within a tissue construct [19]. Combining these methods and materials, with a focus on the optical parameters of the resulting phantoms, would help in moving closer to fully realistic optical mimics of tissue, organ, or full organisms.

#246142 Received 28 Jul 2015; revised 24 Sep 2015; accepted 29 Sep 2015; published 2 Oct 2015

This study represents a step forward in the customization and spatial localization of thermoplastic material with user defined optical properties during 3D printing. While this study focused in creating phantoms suitable for Diffuse Optical Imaging and Spectroscopy applications, including small animal imaging, there is significant potential for optical phantom fabrication with 3D printing technologies for a variety of optical modalities.

Acknowledgments

This study was supported in part by the American Cancer Society (RSG-14-014-01-CCE, to Dr. Darren Roblyer, Boston University), by the NSF (PSF-AIR 1237848, to Dr. Shyam Erramilli, Boston University) and the NIH (R01-CA049248, to Dr. David J. Waxman, Boston University). We also wish to acknowledge the Boston University Photonics Center and the Boston University Biomedical Engineering Senior Design Program.

#246142 Received 28 Jul 2015; revised 24 Sep 2015; accepted 29 Sep 2015; published 2 Oct 2015